



This is a repository copy of *Photoluminescence imaging of single photon emitters within nanoscale strain profiles in monolayer WSe₂*.

White Rose Research Online URL for this paper:

<https://eprints.whiterose.ac.uk/203528/>

Version: Published Version

Article:

Abramov, A.N., Chestnov, I.Y., Alimova, E.S. et al. (6 more authors) (2023)
Photoluminescence imaging of single photon emitters within nanoscale strain profiles in monolayer WSe₂. *Nature Communications*, 14 (1). 5737. ISSN 2041-1723

<https://doi.org/10.1038/s41467-023-41292-9>

Reuse

This article is distributed under the terms of the Creative Commons Attribution (CC BY) licence. This licence allows you to distribute, remix, tweak, and build upon the work, even commercially, as long as you credit the authors for the original work. More information and the full terms of the licence here:

<https://creativecommons.org/licenses/>

Takedown

If you consider content in White Rose Research Online to be in breach of UK law, please notify us by emailing eprints@whiterose.ac.uk including the URL of the record and the reason for the withdrawal request.



eprints@whiterose.ac.uk
<https://eprints.whiterose.ac.uk/>

Photoluminescence imaging of single photon emitters within nanoscale strain profiles in monolayer WSe₂

Received: 9 February 2023

Accepted: 29 August 2023

Published online: 15 September 2023

Check for updates

Artem N. Abramov¹, Igor Y. Chestnov¹, Ekaterina S. Alimova², Tatiana Ivanova¹, Ivan S. Mukhin^{1,3}, Dmitry N. Krizhanovskii⁴, Ivan A. Shelykh^{1,5,6,7}, Ivan V. Iorsh^{1,6,7} & Vasily Kravtsov¹✉

Local deformation of atomically thin van der Waals materials provides a powerful approach to create site-controlled chip-compatible single-photon emitters (SPEs). However, the microscopic mechanisms underlying the formation of such strain-induced SPEs are still not fully clear, which hinders further efforts in their deterministic integration with nanophotonic structures for developing practical on-chip sources of quantum light. Here we investigate SPEs with single-photon purity up to 98% created in monolayer WSe₂ via nanoindentation. Using photoluminescence imaging in combination with atomic force microscopy, we locate single-photon emitting sites on a deep sub-wavelength spatial scale and reconstruct the details of the surrounding local strain potential. The obtained results suggest that the origin of the observed single-photon emission is likely related to strain-induced spectral shift of dark excitonic states and their hybridization with localized states of individual defects.

Single-photon emitters (SPEs) are key elements of rapidly developing quantum technologies as they produce individual photons - basic carriers of quantum information^{1,2}. One of the very promising material platforms for creating SPEs is the family of two-dimensional (2D) van der Waals crystals³. Among them, monolayers of transition metal dichalcogenides (TMDs) hold a special place as direct bandgap semiconductors⁴ with large exciton binding energies⁵ that can host localized SPEs characterized by high brightness, narrow spectral lines, and decent single-photon purity⁶⁻¹⁰.

Due to their 2D nature and unlike traditional bulk semiconductors, TMD monolayers can be easily locally strained, for example, via deformation in the out-of-plane direction^{11,12}. Since the associated excitonic properties are highly strain-dependent, this results in effective local potentials for excitons, providing a powerful approach¹³ towards creating, activating, or tuning SPEs in TMD monolayers with nanostructured substrates and

nanoparticles, piezoelectric devices, or atomic force microscope (AFM) probes¹⁴⁻¹⁸.

In order to enable practical applications of SPEs, their integration with on-chip nanophotonic resonators and waveguides is highly desirable. As previously demonstrated for solid-state SPEs, coupling to optical structures can significantly improve the emission rate, reduce radiative lifetimes, and increase indistinguishability of emitted photons, as well as facilitate their routing into required optical channels via Purcell effect^{19,20}. Similarly, integrating strain-induced SPEs in TMD monolayers with nanophotonic structures allows optimization and control of their emission properties such as directivity and quantum yield as has been demonstrated recently^{21,22}.

However, it is challenging to achieve optimal coupling since SPEs must be placed at the maximum of local optical field distribution. This requires accurate knowledge of the actual SPE position on the nanoscale within a larger strained region of TMD monolayer, which is

¹School of Physics and Engineering, ITMO University, Saint Petersburg 197101, Russia. ²Peter The Great St. Petersburg Polytechnic University, Saint Petersburg 195251, Russia. ³St. Petersburg Academic University, Saint Petersburg 194021, Russia. ⁴Department of Physics and Astronomy, University of Sheffield, Sheffield S3 7RH, UK. ⁵Science Institute, University of Iceland, Dunhagi-3, IS-107 Reykjavik, Iceland. ⁶Abrikosov Center for Theoretical Physics, MIPT, Dolgoprudnyi, Moscow Region, 141701, Russia. ⁷Russian Quantum Center, Skolkovo, Moscow 143025, Russia. ✉e-mail: vasily.kravtsov@metalab.ifmo.ru

not readily available. The issue is further complicated by the fact that the exact mechanisms underlying the formation of strain-induced SPEs in monolayer semiconductors are still not fully clarified. In particular, questions remain about the roles of atomic defects and strain gradients for the SPE formation process²³, as well as possible contributions from bright/dark excitons and hybridization effects²⁴.

Here we experimentally investigate nanoscale positioning and polarization properties of individual SPEs created in monolayer WSe₂ via nanoindentation. The SPEs exhibit excellent single-photon purity with second order correlation function values down to $g^{(2)}(0) \sim 0.02$ and high emission rates of > 1 MHz, which allows us to locate SPEs on a deep subwavelength spatial scale through photoluminescence (PL) imaging. By reconstructing strain distribution maps from the measured AFM topography, we extract local strain tensor components at the exact SPE location and in its vicinity. The observed correlation between the experimentally measured emission properties and theoretically calculated local deformation parameters allows us to conclude on the likely mechanism of SPE formation, which relies on hybridization between dark excitons and localized defect states. Our work establishes a general method for investigating properties of quantum emitters formed in complex 2D nanoscale strain potentials and offers new insights for the future development of practical SPEs based on strained 2D semiconductors for applications in quantum communications and computing.

Results

SPEs with high single-photon purity and brightness

In our experiment, we create strain-induced SPEs in monolayer WSe₂ via nanoindentation with an AFM probe as shown in Fig. 1a, following the general approach demonstrated in Ref. 17. To be able to accurately locate SPE sites on a subwavelength scale, we first fabricate cross-

shaped Ag alignment marks with 1 μm width and 60 nm height on a SiO₂(1 μm)/Si substrate. A thin layer of polymethyl methacrylate (PMMA) is then spun onto the substrate, and a large-scale high-quality WSe₂ monolayer is transferred on top to overlap with the alignment marks as shown in the optical microscope image in Fig. 1b. We create an array pattern of nanoindented regions in the monolayer using a specially modified Si AFM probe (see Supplementary Note 1), where plastic deformation in the PMMA layer in combination with adhesion at the PMMA/WSe₂ interface result in local straining of the monolayer.

For optical measurements, the sample is mounted in a cryostat and maintained at a temperature of 7 K (for setup details, see Methods and Supplementary Note 2). Under focused excitation by a continuous wave HeNe laser with 633 nm wavelength, locally deformed WSe₂ monolayer regions emit PL spectra consisting of bright and narrow spectral lines redshifted with respect to the free neutral exciton peak. Fig. 1c demonstrates an example PL spectrum collected from a selected strained region, where the peak at 710.5 nm is attributed to the free neutral exciton X_b^0 , while peak at 764.4 nm is attributed to a single photon emitter. We observe similar individual spectral lines on more than 50% of all indented regions in the monolayer, with the distribution of their wavelengths covering the range of 720–800 nm and peaked at 750 nm as described later in the text. For a typical emitter, we measure degree of linear polarization of more than 70% (an example of polarization-resolved PL signal is shown in the inset of Fig. 1c), which allows us to maximize the SPE emission intensity with respect to the broader mostly unpolarized PL background (see Supplementary Note 3).

The individual spectral lines in the PL spectra exhibit a saturating dependence on excitation power, which is characteristic of emission from a single two-level system. From the experimentally measured power dependencies of PL intensity, we determine the saturation

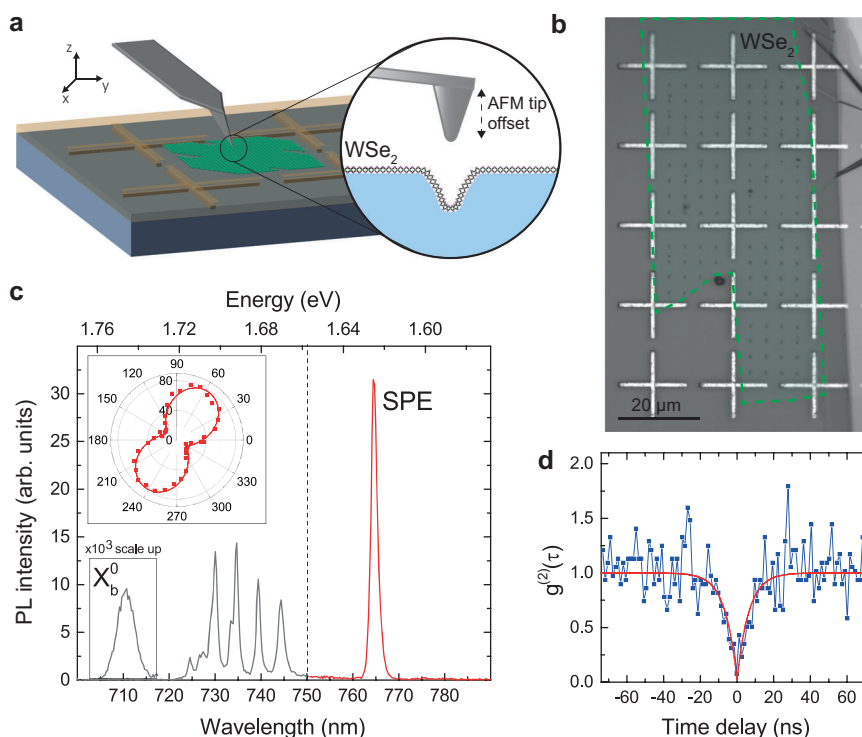


Fig. 1 | Single-photon emission in a locally strained WSe₂ monolayer sample with alignment marks. **a** Schematic of single-photon emitter (SPE) fabrication by nanoindentation in a WSe₂ monolayer transferred onto a substrate with an alignment pattern. **b** Optical image of the sample showing arrays of alignment marks and nanoindents. The WSe₂ monolayer border is highlighted by green dashed line. **c** Photoluminescence (PL) spectrum from a selected SPE. The spectral part

detected in the experiment is highlighted with red color. Spectral peak of the free bright neutral exciton X_b^0 at $\lambda = 710.5$ nm is scaled up by 10^3 . The inset shows typical polarization-resolved spectrally integrated PL signal from an SPE. **d** Second-order correlation function $g^{(2)}(\tau)$ measured for the SPE spectral peak (blue dots) together with fit (red curve), which demonstrates antibunching.

power and corresponding emission rate as outlined in detail in Supplementary Note 4. For most of our measurements, the excitation laser power is chosen slightly below the saturation power and lies in a 0.7–1.0 μW range, which corresponds to emission rates of ~1 MHz limited by relatively low PL quantum yield of 1–4%. We verify the single-photon character of the emitted PL by measuring the second-order autocorrelation $g^{(2)}(\tau)$ as a function of time delay τ in a Hanbury Brown and Twiss setup and fitting the data with $g^{(2)}(\tau) = 1 - (1 - A)e^{-|\tau|/\tau_0}$, where A and τ_0 are fit parameters, and there are no corrections for background or dark counts. The extracted values of τ_0 are roughly of the same order as the SPE PL decay times lying in a 1–20 ns range. All extracted values of $A = g^{(2)}(0)$ are below 0.4, and a significant portion of them are below 0.1 for individual redshifted PL peaks from different indented regions, confirming the single-photon nature of the corresponding localized emitters. While the average value of $g^{(2)}(0)$ in our statistics is 0.15 ± 0.12 (see Supplementary Note 5), some emitters exhibit significantly smaller values down to $g^{(2)}(0) \simeq 0.02$ as demonstrated in Fig. 1d, which shows experimental $g^{(2)}(\tau)$ data (blue dots) together with a corresponding fit (red line). We note that the estimated single-photon purity of 98% is among the highest reported for SPEs in atomically thin semiconductors to date.

SPE coordinates within nanoscale strain profiles

While each fabricated locally strained region in monolayer WSe_2 extends over $0.5 \mu\text{m}$, the SPEs are expected to be point-like and localized at well-defined sites within the strain profiles. To accurately locate the SPEs, we use the PL-imaging approach that has been previously applied for single molecules and individual solid-state semiconductor quantum dots^{25,26}. The approach is based on fitting the real-space PL image of the SPE with a point spread function to determine the SPE coordinates with respect to alignment marks. We excite individual strained regions and select corresponding SPE PL signals via spectral (wavelength $> 750 \text{ nm}$, red color in Fig. 1c) and polarization filtering. The sample is simultaneously illuminated by white light from a lamp spectrally filtered with a 10 nm band pass filter to detect reflected optical signal from the Ag alignment marks, and both PL and reflected images of the sample are captured by a CMOS camera.

Fig. 2a shows a selected camera image, where the bright circle corresponds to the PL signal from a strain-induced SPE in monolayer WSe_2 . To determine the coordinates of the SPE and alignment marks, we take line cuts from the camera image along horizontal (X) and vertical (Y) directions, with the background-subtracted data shown in Fig. 2b and c (dots). We note that the relative intensities of the peaks shown in Fig. 2b, c are controlled by the intensity of the alignment mark illumination and chosen to maximize corresponding signal-to-noise ratios and minimize the uncertainty in the coordinate extraction procedure. While the spatial distribution of PL from a single point emitter in an ideal visualization system follows the Airy function, we use Gauss functions as a good approximation for their central parts, which is more convenient for data processing^{25,27}. From Gaussian fits of the marks (blue curves) and SPE (red curves) profiles, we extract the X and Y coordinates as peak centers together with corresponding uncertainties as fit errors. The uncertainties of the $X(Y)$ coordinates for the fits shown in Fig. 2b and c are obtained as 5.5 nm (6.6 nm) for the SPE and 7.9 nm (13.3 nm) for the alignment mark.

Next, we map the extracted coordinates onto the AFM topography image of the sample shown in Fig. 2d. We determine the coordinates of the alignment marks in the AFM image, match them to the corresponding coordinates in the optical image, obtain the associated transformation matrix, and use it to locate the SPE site on the AFM map. We note that despite the presence of the PMMA layer, the alignment marks create enough protrusion at the surface to allow extracting their center X and Y coordinates with accuracy of 1.6 nm and 3.4 nm, respectively, as shown in Fig. 2e and f. Based on the uncertainties obtained for SPE and alignment marks coordinates in the

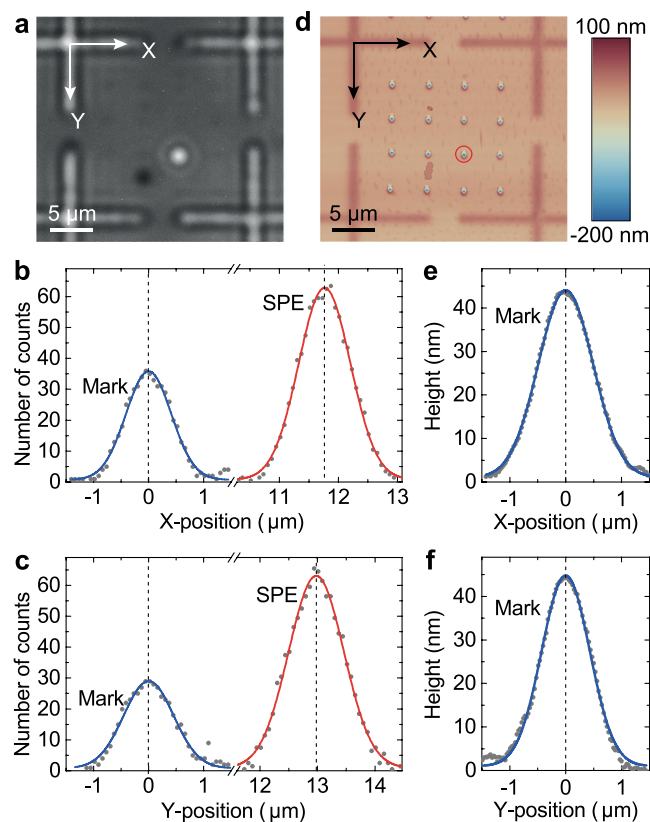


Fig. 2 | Measurement of SPE position with subwavelength accuracy. **a** Optical image acquired by illuminating the sample simultaneously by a HeNe laser and 10 nm band pass filtered light from a halogen lamp. The circular spot corresponds to PL from an SPE. **b, c** Selected X- and Y-line cuts of the camera image taken through the alignment mark and SPE (dots), with respective Gaussian fits (blue and red curves). Signals are not normalized. **d** AFM topography image of the same region, with the red circle indicating the laser-illuminated nanoindent. Color scale represents the height. **e, f** Selected X- and Y-line cuts of the AFM scan taken through the alignment mark, with Gaussian fits (blue curves). Vertical dashed lines indicate the extracted coordinates.

optical and AFM images we estimate the expected uncertainty of the SPE position on the AFM map as ~22(28) nm for the $X(Y)$ coordinates. Further, we take a sequence of PL images and calculate the experimental uncertainty as the standard deviation of the extracted SPE position, which gives ~30(13) nm for the $X(Y)$ coordinates of the SPE shown in Fig. 2, consistent with the estimated values. The extracted uncertainties are likely limited by the residual vibrations and drift in our cryostat system and can be reduced down to 10–20 nm in a setup with improved stability. We note that an additional uncertainty can in principle be present due to the different sample temperatures for the optical and AFM measurements and the associated thermal expansion. However, for the materials and characteristic alignment grid sizes used in our experiment the potential distortions are estimated to be below 10 nm.

The AFM scan of a single nanoindent along with the identified SPE location are shown in Fig. 3a. Surprisingly, the SPE appears at the outer slope of the fold wrapped around the indentation area rather than in the center of the nanoindent. Similar results are observed for other studied SPEs in our sample (see Supplementary Note 6 and Fig. 4). These observations do not align well with the common interpretation of the SPE origin in TMD monolayers relying on strain-induced nanoscale trapping of excitons^{14,15,28–30}. While exciton trapping is expected at the energy minima of the strain-induced potential, that is, at the maxima of the local tensile strain, the SPEs in our experiment are

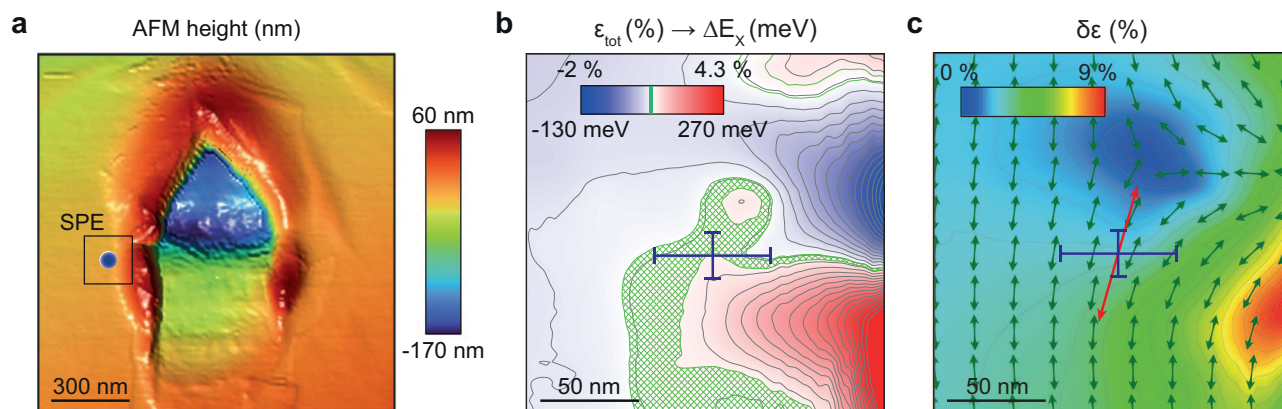


Fig. 3 | Analysis of local strain in the vicinity of the SPE site. **a** AFM topography of the strained region with the experimentally extracted SPE location indicated with a blue circle. **b** Calculated from the AFM topography total in-plane strain ϵ_{tot} (false color scale in %), which translates into exciton transition energy shift ΔE_x (scale in meV). The region shown corresponds to the area indicated with a black rectangle in (a), and the SPE location together with experimental uncertainties obtained from a series of measurements are shown with the blue error bars

in the green-shaded region, the calculated strain-shifted dark exciton energy matches the SPE energy. **c** Calculated spatial distribution of the local strain difference along the principal axes $\delta\epsilon$ (false color image) quantifying the strain asymmetry, together with the calculated orientation of the principal strain axis corresponding to the lowest-energy state of the exciton radiative doublet (green arrows). The SPE location and polarization direction are indicated with blue error bars and long red arrow, respectively.

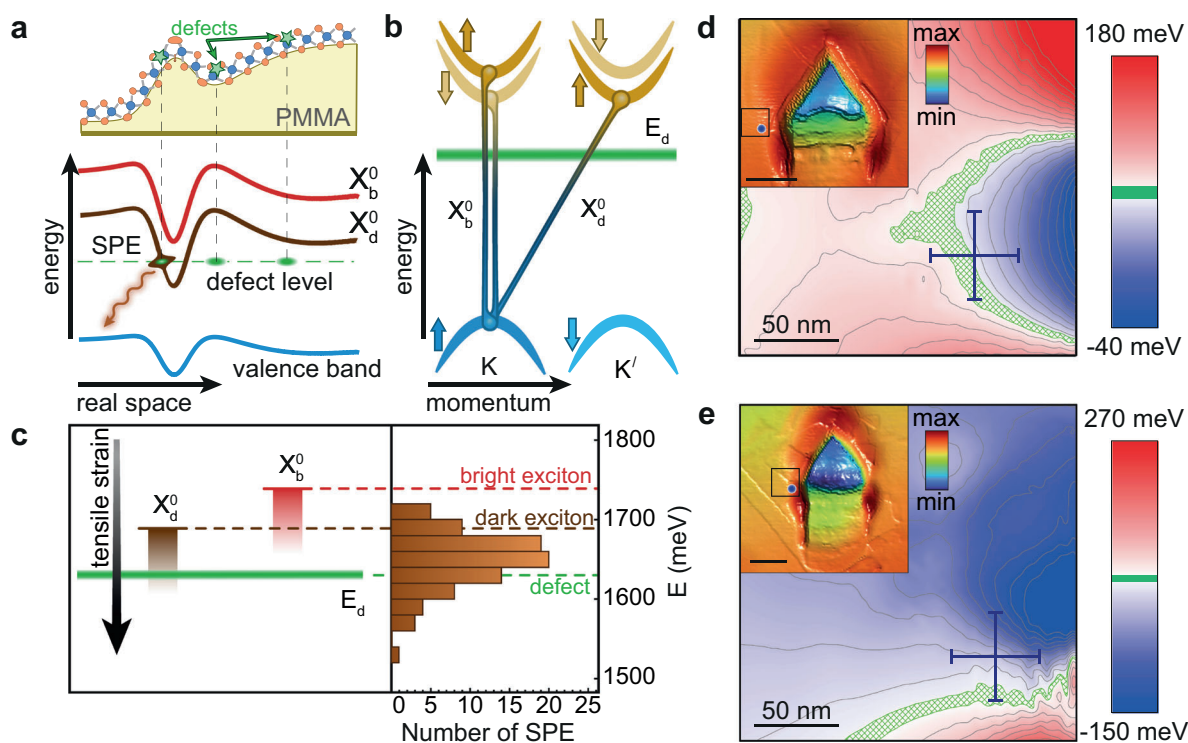


Fig. 4 | Single-photon emission mechanism in strained monolayer WSe₂.

a Spatial variation of the exciton energy due to nonuniform strain distribution in the deformed monolayer. Both bright X_b^0 and dark X_d^0 exciton bands are redshifted in the region of local tensile strain. The SPE originates from hybridization of the dark exciton with the mid-gap defect state (indicated by green circles) when they come in resonance (the defect energy is indicated by the horizontal green dashed line, and photon emission process is indicated by the wavy red arrow). **b** Schematic illustration of the dark intervalley exciton formed in monolayer WSe₂ between the K and K' valleys, with arrows indicating spin states. Mid-gap defect level is shown with green line. **c** Right panel: measured distribution of SPE energies for a large

ensemble of emitters. Left panel: schematic illustration for the spectral positions of the free bright X_b^0 , dark X_d^0 , and the localized defect E_d exciton states shown by dashed horizontal lines, with the expected effect of the strain-induced redshift (indicated by red and brown gradient shaded areas). **d, e** Maps of the total in-plane strain ϵ_{tot} near 2 additional SPE sites, with AFM topography images in the inset (AFM scale bar is 300 nm, color scale represents the height). In the green-shaded regions, the calculated strain-shifted dark exciton energy matches the SPE energy. The experimental uncertainties for extracted SPE coordinates obtained from a series of measurements are indicated with blue error bars.

located far from the strain maxima. We note that a similar trend has been recently observed for strain-induced SPEs in WS_2^{31} .

Calculation of the local strain tensor components

To understand the possible origin of the studied SPEs, we analyze the local strain distribution in the nanoindent vicinity. In 2D crystals, the strain can be described by the in-plane tensor $\hat{\epsilon}^{32}$:

$$\epsilon_{ij} = \frac{1}{2} (\partial_i u_j + \partial_j u_i + \partial_i h \partial_j h). \quad (1)$$

Here $i, j = x, y$, and $\mathbf{u}(\mathbf{r}) = (u_x(\mathbf{r}), u_y(\mathbf{r}))^T$ stands for the in-plane displacement vector, while $h(\mathbf{r})$ is the out-of-plane deformation profile known from the AFM data. In the absence of external in-plane forces, the $\mathbf{u}(\mathbf{r})$ -dependence can be retrieved from the equilibrium condition $\nabla \cdot \hat{\sigma} = 0$ and the Hooke's law

$$\begin{pmatrix} \sigma_{xx} \\ \sigma_{yy} \end{pmatrix} = \frac{E}{1-\nu^2} \begin{pmatrix} 1 & \nu \\ \nu & 1 \end{pmatrix} \begin{pmatrix} \epsilon_{xx} \\ \epsilon_{yy} \end{pmatrix}, \quad \sigma_{xy} = \frac{E}{1+\nu} \epsilon_{xy}. \quad (2)$$

Here $\hat{\sigma}$ is the stress tensor and $\nabla = (\partial_x, \partial_y)$ is a divergence row-vector, E is the 2D Young's modulus and ν is the Poisson's ratio^{33,34}. From combined Eqs. (1) and (2), we obtain an equation for the displacement vector $\mathbf{u}(\mathbf{r})$, solve it, and finally calculate the full strain tensor $\hat{\epsilon}(\mathbf{r})$ as a function of the in-plane coordinate \mathbf{r} according to Eq. (1) (for more detailed description of the calculation procedure, see Methods and Supplementary Note 7).

From the calculated strain tensor, we extract spatial distributions in the vicinity of the SPE site for the following three parameters: (i) total in-plane strain $\epsilon_{\text{tot}} = \epsilon_{xx} + \epsilon_{yy}$ plotted in Fig. 3b, (ii) orientation θ of the principal strain axis plotted in Fig. 3c with green arrows, and (iii) strain difference along the principal axes $\delta\epsilon$ plotted in Fig. 3c as a false-color map. The region shown in Fig. 3b, and c is a zoomed-in area indicated with a black rectangle in Fig. 3a. The experimentally extracted SPE location is indicated with a blue circle in Fig. 3a and with blue error bars in Fig. 3b and c.

Discussion

We first discuss the results for parameters θ and $\delta\epsilon$, which are associated with the anisotropy of local strain fields (see Methods for calculation details). In monolayer TMDs, anisotropic strain breaks the chiral selection rules and results in a radiative excitonic doublet with emission linearly polarized in two orthogonal directions defined by the principal strain axes^{7,35,36}. Consistent with this theoretical expectation, our experimentally measured linear polarization direction for the SPE indicated in Fig. 3c with a red arrow is found to coincide with the principal strain axis (green arrows) within the spatial area defined by the experimental uncertainty for the SPE location (blue error bars for X and Y uncertainties). On the other hand, our SPE spectral peaks do not exhibit fine-structure splitting and emit photons in a single dominant linear polarization. This is similar to results reported previously for structures with strong asymmetry such as nanowrinkles or artificial quasi-1D confinement potentials where PL is linearly polarized along the elongated direction^{37–40}. We estimate the expected fine-structure splitting of the SPE spectral peak from local strain anisotropy governed by $\delta\epsilon$. As observed in Fig. 3c, the strain difference $\delta\epsilon$ at the SPE location is $\sim 2.4\%$, which translates to ~ 2.4 meV strain-induced contribution to the exciton fine-structure splitting if we use the estimate of 1 meV/% from Ref. 35. This is similar to the linewidth of our emitters of 2–3 meV (see Supplementary Note 5), which makes it challenging to distinguish the split peaks in the measurements. Additionally, at the temperature of 7 K, and taking into account relatively long measured lifetimes on the ns scale, the lower-energy level in the doublet will be populated predominantly, which might also explain the absence of SPE peak splitting in our experimentally obtained data. We note that this is

consistent with the experimental observation that the SPE polarization matches the principal axis corresponding to the lowest-energy state (green arrows in Fig. 3c) in the radiative doublet.

Next, we discuss the results for the total strain ϵ_{tot} with calculated spatial distribution in the vicinity of the SPE site shown in Fig. 3b (false color scale in %). Assuming that the energy bandgap depends linearly on the total in-plane strain and that the exciton binding energy is affected only weakly, we calculate the expected shift of the exciton transition energy as $\Delta E_X = \alpha \epsilon_{\text{tot}}$, where $\alpha = 63$ meV/% is the estimate for the energy shift rate for monolayer WSe_2 taken from Ref. 34. As observed in Fig. 3b, the spatial distribution of the strain-induced energy shift (false color scale in meV) does not exhibit relevant conditions for exciton trapping. The quantum confinement of excitons can be expected to emerge under the strain modulation on the order of 1% within 10 nm length scale⁴¹, while the extracted energy landscape appears to be smooth on a significantly larger spatial scale (less than 0.05% within 10 nm). In addition, the strain-free energy of $E - 1.703$ eV estimated from the redshift due to deformation (~ 78 meV) at position of the SPE with wavelength of 763 nm (1.625 eV) turns out to be far from the strain-free bright exciton energy $E_{Xb} = 1.745$ eV.

These observations suggest that strain-induced trapping of bright excitons is an unlikely SPE formation mechanism in our experiment. Instead, they are consistent with the hypothesis that attributes SPE formation to the strain-induced resonant hybridization of optically dark excitons with point-like defects as discussed in recent works^{23,24,42}. The proposed single-photon emission mechanism is schematically illustrated in Fig. 4a and relies on brightening of optically dark excitons (X_d^0) when scattering on the individual point-like defects (green dots) present in the WSe_2 monolayer. To enable the brightening process, the dark exciton (X_d^0 , brown curve) should come in resonance with the defect level (green dashed line), which is achieved via strain-induced energy shift. While the energy of a defect level is almost independent of strain⁴², the dark exciton energy follows the local variation of the bandgap and matches the defect energy at certain values of total in-plane strain resulting in a possible photon emission event (wavy arrow).

We note that the dark excitons involved in this mechanism are likely *intervalley* excitons composed of the same-spin valence and conduction band states from the neighboring valleys, see Fig. 4b. In WSe_2 the dark intervalley exciton X_d^0 lies ~ 45 meV below the bright exciton X_b^0 ^{43,44} and almost coincides in energy with the spin-forbidden intravalley dark exciton^{33,34,45}. However, brightening of intravalley dark excitons is less likely as it requires an additional spin flip process. The defects involved in the brightening process are likely the omnipresent Se vacancies²³, with corresponding energy levels lying several tens of meV below the dark exciton in monolayer WSe_2 ^{24,42}. Our experimentally measured distribution of SPE energies obtained from a large ensemble of > 80 emitters shown in Fig. 4c (right panel) supports this assignment as it is peaked near 1.63 eV corresponding to the expected spectral position of the mid-gap Se-vacancy defect⁴². The relatively large width of the SPE energy distribution agrees with the results of recent experimental studies on statistics of emitters in WSe_2 monolayer^{46,47} and reports on dark-localized exciton mixing in the wide spectral range around the defect energy level⁴².

As schematically illustrated in the left panel of Fig. 4c, the local strain at the SPE site brings the energy of the dark exciton (X_d^0) in resonance with the defect level. This is indeed what is observed in our data shown in Fig. 3b. There we highlight with green color the spatial region where the strain-induced energy redshift falls within the range 68–78 meV, corresponding to the difference between the energies of the given SPE (1.625 eV) and dark intervalley exciton (~ 1.70 eV) in monolayer WSe_2 . Analogous data extracted for two other SPEs are shown in Fig. 4d (64–74 meV redshift) and e (53–63 meV redshift), together with corresponding AFM images with indicated extracted SPE locations (insets). All three plots demonstrate that SPEs are located at

or very near the corresponding green-highlighted regions where the difference between the SPE and dark exciton energies is equal to the strain-induced energy redshift. The data for the set of emitters are summarized in Supplementary Note 8. Analysis of the SPE brightness demonstrates that the emission intensity is maximized near 1.63 eV where the SPE energy matches the expected Se-vacancy energy level⁴². These observations, together with the lack of evidence for bright exciton trapping in our experimental data and theoretical analysis, render the resonant hybridization of dark excitons with individual atomic defects a favorable explanation of SPE formation in our strained samples of monolayer WSe₂.

In summary, we have investigated the precise nanoscale distribution of mechanical strain in the vicinity of single-photon emitting sites fabricated via nanoindentation in monolayer WSe₂ using combined PL and AFM imaging. The high single-photon purity and brightness of the fabricated SPEs allowed us to locate them within the strained region with subwavelength accuracy on the order of tens of nm. To obtain insights into the SPE formation mechanism, we provide a model for calculating the full strain tensor at and near the determined SPE location. Our analysis and comparison of the experimentally measured data and extracted components of the local strain tensor shows that the single-photon emission in our case likely relies on brightening of dark excitonic states on individual point-like defects in the monolayer, rather than on formation of quantized excitonic levels due to exciton trapping. The obtained results provide important insights into the microscopic mechanisms governing single-photon emission in 2D semiconductors and contribute towards further integration of SPEs in TMD monolayers with nanophotonic resonators and waveguides.

Methods

Sample preparation

Ag alignment marks are fabricated on a SiO₂(1 μm)/Si substrate using electron-beam lithography with double PMMA layer followed by thermal evaporation of 2 nm/60 nm Cr/Ag and lift-off in ultrasound with acetone. The marks form a grid of 4 × 4 squares of 20 × 20 μm² each and are covered with a 300 nm PMMA layer. WSe₂ monolayers are obtained from a bulk crystal by mechanical exfoliation and transferred onto the PMMA surface using standard dry transfer. Nanoindents in WSe₂ monolayer with depth of 100–200 nm are formed using silicon AFM probe blunted with a focused ion beam.

PL-imaging approach

To obtain a PL image, the sample is illuminated with HeNe laser to excite photoluminescence and lamp light with a bandpass filter to illuminate alignment marks. The signal is collected by a 50 × long working distance Mitutoyo objective (NA = 0.65) mounted on a three-axis piezoelectric translator for the precise positioning of the laser spot. Data acquisition time and lamp brightness are optimized to obtain similar number of counts for the SPE PL and reflection signal from the alignment marks, as well as to minimize the reflection of the lamp light from the substrate and minimize possible sample drift during measurement.

Strain analysis

The strain profile is obtained from the solution of the equilibrium equation $\nabla \cdot \hat{\sigma} = 0$ for the in-plane displacement vector \mathbf{u} using finite element method with $\nu = 0.196$ ^{33,34}. Orientation of the principal strain axes is obtained by diagonalizing the strain tensor at every point of the AFM scan grid. This requires rotation at the angle θ given by $\tan(2\theta) = 2\epsilon_{xy}/(\epsilon_{xx} - \epsilon_{yy})$ which eliminates shear strain and brings $\hat{\epsilon}$ to the diagonal form. The difference of the principal strains $\delta\epsilon = \sqrt{(\epsilon_{xx} - \epsilon_{yy})^2 + 4\epsilon_{xy}^2}$ governs the fine-structure splitting with the rate Δ_{fs} whose value is assumed to be below 1 meV per percent of strain according to the estimations for the bright exciton doublet in WSe₂³⁵. The vector map in Fig. 3c corresponds to the principal strain of the

state defined by the strain tensor eigenvector $(-\sin(\theta), \cos(\theta))^T$ which corresponds to the lowest in energy state of the fine-structure doublet. This state is expected to dominate polarization properties of the SPE.

Data availability

The data that support the findings of this study are available within the main text and Supplementary Information. Any other relevant data are available from the corresponding authors upon request.

References

- Aharonovich, I., Englund, D. & Toth, M. Solid-state single-photon emitters. *Nat. Photonics* **10**, 631–641 (2016).
- Eisaman, M. D., Fan, J., Migdall, A. & Polyakov, S. V. Invited review article: Single-photon sources and detectors. *Rev. Sci. Instrum.* **82**, 071101 (2011).
- Toth, M. & Aharonovich, I. Single photon sources in atomically thin materials. *Annu. Rev. Phys. Chem.* **70**, 123–142 (2019).
- Kumar, A. & Ahluwalia, P. Electronic structure of transition metal dichalcogenides monolayers 1H-MX₂ (M=Mo, W; X=S, Se, Te) from ab-initio theory: new direct band gap semiconductors. *Eur. Phys. J. B* **85**, 186 (2012).
- Mueller, T. & Malic, E. Exciton physics and device application of two-dimensional transition metal dichalcogenide semiconductors. *npj 2D Mater. Appl.* **2**, 29 (2018).
- Chakraborty, C., Kinnischtzke, L., Goodfellow, K. M., Beams, R. & Vamivakas, A. N. Voltage-controlled quantum light from an atomically thin semiconductor. *Nat. Nanotechnol.* **10**, 507–511 (2015).
- He, Y.-M. et al. Single quantum emitters in monolayer semiconductors. *Nat. Nanotechnol.* **10**, 497–502 (2015).
- Koperski, M. et al. Single photon emitters in exfoliated WSe₂ structures. *Nat. Nanotechnol.* **10**, 503–506 (2015).
- Srivastava, A. et al. Optically active quantum dots in monolayer WSe₂. *Nat. Nanotechnol.* **10**, 491–496 (2015).
- Tonndorf, P. et al. Single-photon emission from localized excitons in an atomically thin semiconductor. *Optica* **2**, 347–352 (2015).
- He, K., Poole, C., Mak, K. F. & Shan, J. Experimental demonstration of continuous electronic structure tuning via strain in atomically thin MoS₂. *Nano Lett.* **13**, 2931–2936 (2013).
- Benimetskiy, F. et al. Measurement of local optomechanical properties of a direct bandgap 2D semiconductor. *APL Mater.* **7**, 101126 (2019).
- Ren, S., Tan, Q. & Zhang, J. Review on the quantum emitters in two-dimensional materials. *J. Semicond.* **40**, 071903 (2019).
- Branny, A., Kumar, S., Proux, R. & Gerardot, B. D. Deterministic strain-induced arrays of quantum emitters in a two-dimensional semiconductor. *Nat. Commun.* **8**, 15053 (2017).
- Iff, O. et al. Strain-tunable single photon sources in WSe₂ monolayers. *Nano Lett.* **19**, 6931–6936 (2019).
- Peng, L. et al. Creation of single-photon emitters in WSe₂ monolayers using nanometer-sized gold tips. *Nano Lett.* **20**, 5866–5872 (2020).
- Rosenberger, M. R. et al. Quantum calligraphy: writing single-photon emitters in a two-dimensional materials platform. *ACS Nano* **13**, 904–912 (2019).
- Li, X. et al. Proximity induced chiral quantum light generation in strain-engineered WSe₂/NiPS₃ heterostructures. *arXiv preprint arXiv:2203.00797* (2022).
- Liu, F. et al. High purcell factor generation of indistinguishable on-chip single photons. *Nat. Nanotechnol.* **13**, 835–840 (2018).
- Lodahl, P., Mahmoodian, S. & Stobbe, S. Interfacing single photons and single quantum dots with photonic nanostructures. *Rev. Mod. Phys.* **87**, 347 (2015).
- Sortino, L. et al. Bright single photon emitters with enhanced quantum efficiency in a two-dimensional semiconductor coupled with dielectric nano-antennas. *Nat. Commun.* **12**, 6063 (2021).

22. Iff, O. et al. Purcell-enhanced single photon source based on a deterministically placed WSe₂ monolayer quantum dot in a circular Bragg grating cavity. *Nano Lett.* **21**, 4715–4720 (2021).
23. Parto, K., Azzam, S. I., Banerjee, K. & Moody, G. Defect and strain engineering of monolayer WSe₂ enables site-controlled single-photon emission up to 150 K. *Nat. Commun.* **12**, 3585 (2021).
24. Linhart, L. et al. Localized intervalley defect excitons as single-photon emitters in WSe₂. *Phys. Rev. Lett.* **123**, 146401 (2019).
25. Thompson, R. E., Larson, D. R. & Webb, W. W. Precise nanometer localization analysis for individual fluorescent probes. *Biophys. J.* **82**, 2775–2783 (2002).
26. Sapienza, L., Davanço, M., Badolato, A. & Srinivasan, K. Nanoscale optical positioning of single quantum dots for bright and pure single-photon emission. *Nat. Commun.* **6**, 7833 (2015).
27. Saxton, M. J. & Jacobson, K. Single-particle tracking: applications to membrane dynamics. *Annu. Rev. Biophys. Biomol. Struct.* **26**, 373–399 (1997).
28. Darlington, T. P. et al. Imaging strain-localized excitons in nanoscale bubbles of monolayer WSe₂ at room temperature. *Nat. Nanotechnol.* **15**, 854–860 (2020).
29. Shepard, G. D. et al. Nanobubble induced formation of quantum emitters in monolayer semiconductors. *2D Mater.* **4**, 021019 (2017).
30. Palacios-Berraquero, C. et al. Large-scale quantum-emitter arrays in atomically thin semiconductors. *Nat. Commun.* **8**, 15093 (2017).
31. Cianci, S. et al. Spatially controlled single photon emitters in hBN-capped WS₂ domes. *Adv. Opt. Mater.* **11**, 2202953 (2023).
32. Landau, L. D., Lifshitz, E. M., Kosevich, A. M. & Pitaevskii, L. P. *Theory of elasticity* (Elsevier, 1986).
33. Zeng, F., Zhang, W.-B. & Tang, B.-Y. Electronic structures and elastic properties of monolayer and bilayer transition metal dichalcogenides MX₂ (M = Mo, W; X = O, S, Se, Te): a comparative first-principles study. *Chin. Phys. B* **24**, 097103 (2015).
34. Blundo, E., Cappelluti, E., Felici, M., Pettinari, G. & Polimeni, A. Strain-tuning of the electronic, optical, and vibrational properties of two-dimensional crystals. *Appl. Phys. Rev.* **8**, 021318 (2021).
35. Glazov, M. et al. Exciton fine structure splitting and linearly polarized emission in strained transition-metal dichalcogenide monolayers. *Phys. Rev. B* **106**, 125303 (2022).
36. Kim, H., Moon, J. S., Noh, G., Lee, J. & Kim, J.-H. Position and frequency control of strain-induced quantum emitters in WSe₂ monolayers. *Nano Lett.* **19**, 7534–7539 (2019).
37. Alexeev, E. M. et al. Emergence of highly linearly polarized interlayer exciton emission in MoSe₂/WSe₂ heterobilayers with transfer-induced layer corrugation. *ACS Nano* **14**, 11110–11119 (2020).
38. Wang, Q. et al. Highly polarized single photons from strain-induced quasi-1D localized excitons in WSe₂. *Nano Lett.* **21**, 7175–7182 (2021).
39. So, J.-P. et al. Polarization control of deterministic single-photon emitters in monolayer WSe₂. *Nano Lett.* **21**, 1546–1554 (2021).
40. Kern, J. et al. Nanoscale positioning of single-photon emitters in atomically thin WSe₂. *Adv. Mater.* **28**, 7101–7105 (2016).
41. Chirulli, L., Prada, E., Guinea, F., Roldán, R. & San-Jose, P. Strain-induced bound states in transition-metal dichalcogenide bubbles. *2D Mater.* **6**, 025010 (2019).
42. Hernández López, P. et al. Strain control of hybridization between dark and localized excitons in a 2D semiconductor. *Nat. Commun.* **13**, 7691 (2022).
43. Zhang, X.-X. et al. Magnetic brightening and control of dark excitons in monolayer WSe₂. *Nat. Nanotechnol.* **12**, 883–888 (2017).
44. Barbone, M. et al. Charge-tunable biexciton complexes in monolayer WSe₂. *Nat. Commun.* **9**, 3721 (2018).
45. Liu, E. et al. Multipath optical recombination of intervalley dark excitons and trions in monolayer WSe₂. *Phys. Rev. Lett.* **124**, 196802 (2020).
46. Moon, H. et al. Strain-correlated localized exciton energy in atomically thin semiconductors. *ACS Photonics* **7**, 1135–1140 (2020).
47. Luo, Y., Liu, N., Kim, B., Hone, J. & Strauf, S. Exciton dipole orientation of strain-induced quantum emitters in WSe₂. *Nano Lett.* **20**, 5119–5126 (2020).

Acknowledgements

This research was supported by Priority 2030 Federal Academic Leadership Program. The authors acknowledge funding from Ministry of Science and Higher Education of Russian Federation, goszadanie no. 2019-1246. The work of I.V.I. was supported by Rosatom in the framework of the Roadmap for Quantum computing (Contract No. 868-1.3-15/15-2021 dated October 5). I.A.S. acknowledges support from the Icelandic Research Fund (Project “Hybrid polaritonics”). This work was carried out using equipment of the SPbU Resource Centers “Nanophotonics” and “Nanotechnology”. We thank Mikhail Glazov and Ekaterina Khestanova for fruitful discussions.

Author contributions

A.N.A., I.V.I. and V.K. conceived the idea and designed the experiment. A.N.A. and T.I. fabricated TMD monolayers. A.N.A. and I.S.M. fabricated nanoindentors and alignment grids. A.N.A. fabricated and characterized SPE arrays. A.N.A. and E.S.A. performed optical measurements. I.Y.C. and I.V.I. developed theoretical model and performed calculations. A.N.A., I.Y.C. and V.K. wrote the manuscript. A.N.A., I.Y.C., D.N.K., I.A.S., I.V.I. and V.K. discussed and interpreted the results. V.K. supervised the project.

Competing interests

The authors declare no competing interests.

Additional information

Supplementary information The online version contains supplementary material available at <https://doi.org/10.1038/s41467-023-41292-9>.

Correspondence and requests for materials should be addressed to Vasily Kravtsov.

Peer review information *Nature Communications* thanks the anonymous reviewer(s) for their contribution to the peer review of this work. A peer review file is available.

Reprints and permissions information is available at <http://www.nature.com/reprints>

Publisher's note Springer Nature remains neutral with regard to jurisdictional claims in published maps and institutional affiliations.

Open Access This article is licensed under a Creative Commons Attribution 4.0 International License, which permits use, sharing, adaptation, distribution and reproduction in any medium or format, as long as you give appropriate credit to the original author(s) and the source, provide a link to the Creative Commons licence, and indicate if changes were made. The images or other third party material in this article are included in the article's Creative Commons licence, unless indicated otherwise in a credit line to the material. If material is not included in the article's Creative Commons licence and your intended use is not permitted by statutory regulation or exceeds the permitted use, you will need to obtain permission directly from the copyright holder. To view a copy of this licence, visit <http://creativecommons.org/licenses/by/4.0/>.

© The Author(s) 2023